Simulation of the deformable lateral boundaries in biaxial test using DEM

Ali Momeni[1,2], Barry Clarke[3], Yong Sheng[4] and Ali Hassapour[5*]

1. **WSP, 3 Wellington Pl, Leeds LS1 4AP, UK; Ali.Momeni@WSP.com**
2. **Visiting Academic at Hull University, Hull, HU6 7RX, UK, A.Momeni@hull.ac.uk**
3. **School of School of Civil Engineering, Leeds LS2 9JT, UK**
   B.G.Clarke@leeds.ac.uk
4. **School of Computer Science, University of Hull, Hull, HU6 7RX, UK**
   y.sheng@hull.ac.uk
5. **School of Chemical and Process Engineering, University of Leeds, Leeds LS2 9JT, UK,**
   A.Hassanpour@leeds.ac.uk

* Corresponding author: A.Hassanpour@leeds.ac.uk; Tel.: 01133432405

Abstract

The use of the discrete element method (DEM) to study soil mechanics' problems at particle level opens a new window to enhance our understanding of the mechanical behaviour of soil. This method can provide abundant information at the particle-scale and can be used as a powerful tool to illustrate the macro-mechanical behaviour of soils based on the inter-particle mechanisms. The triaxial test is one of the most common laboratory methods to study the macro-mechanical behaviour of particulate materials such as soil. However, many problems in geotechnical design can be assumed and simplified as a plane strain problem. Therefore a biaxial test can be conducted to reproduce the macro-mechanical behaviour of soil, where the sample is enclosed by two horizontal rigid platens and a vertical latex membrane, which is a deformable continuous element and allowing the enclosed specimen to deform freely while maintaining confining stress during loading. This paper presents an algorithm to represent physical and mechanical characteristics of latex membrane in the 2D DEM simulation of biaxial test using the PFC^{2D} code. To investigate the impact of the lateral boundary conditions on micro-macro mechanical behaviour of soil samples, two sets of DEM biaxial tests are considered with rigid and deformable lateral boundary conditions. The DEM modeling results indicate that the lateral boundary conditions have a significant effect on the micro-scale fabric properties, thickness and inclination of the shear band. The comparison between these two simulations also demonstrates that the lateral boundary conditions play a major role in the peak and post-peak stress-strain behaviour as well as the dilation and critical state behaviour of granular soils.

Keywords: Discrete Element Method, Biaxial test, Deformable boundaries, Shear band, Critical state, Fabric Anisotropy, Geometrical Stability Index

1. Introduction

The triaxial test is the most common laboratory method applied on the soil element to determine stress strain characteristics [1, 2]. This information is produced by monitoring the imposed displacement and pressure over the boundaries of the sample. Many problems in geotechnical design, however, are

assumed to be plane strain [3, 4]. That is, studying the soil behaviour through two-dimensional laboratory tests such as biaxial test can be more appropriate. In a biaxial test, the granular soil is bounded with four boundaries: two horizontal rigid platens and two vertical membranes which allow the particulate system to deform freely during shearing, while maintaining a specified confining condition. However, applying such laboratory test on the granular soil is not fully addressed in the literature. Alternatively, a two-dimensional simulation, for instance using Discrete Element Method (DEM), can be applied to analyse this test. Since the response of granular soils, such as stress and strain to the applied load in this test is only measured over the boundaries of sample, simulating the proper boundary condition using DEM plays a major role in the macro mechanical behaviour of particulate system during testing. The use of DEM to simulate and analyse the problems in the geomechanics field has been increasing [5, 6, 7]. It has been proven that DEM is a powerful numerical tool to study the micro and macro scales of granular soils by providing abundant information at the particle scale such as inter-particle interactions, particle velocities, displacements and rotations that might not be measured in the laboratory tests. Many researchers, the most notable [8, 9, 10], have illustrated that an invaluable insight can be attained from considering two-dimensional models of idealized soil. A series of DEM biaxial tests on intact rock with rigid boundary condition were performed for comparison and calibration purposes with standard triaxial test data from the laboratory [11, 12]. The most notable DEM biaxial test on idealized soil with edge bounded particles were implemented by Oda et. al [13] and Kawamoto et. al [14]. This method can result in developing the bending stiffness which has an impact on the bulk responses of the particulate systems. Additionally, the boundary particles cannot freely move during loading. Chung and O'Sullivan [41] have introduced an algorithm to simulate deformable boundaries. In their work, boundary particles are able to move, while limited by a confining pressure. In this paper, we have made some improvements in the algorithm to model the continuous membrane for lateral boundaries of biaxial test as deformable boundaries [15]. The modified algorithm, which is described in detail in section 6 of this paper, is used to investigate the sensitivity of the macro-mechanical behaviour of soil as well as the fabric evolution to the lateral boundary conditions: rigid boundaries and deformable boundaries.

2. DEM implementation in PFC^{2D}

DEM is an advanced numerical algorithm which was originally proposed by Cundall and Strack [5]. It can dynamically simulate and track the micro-macro scale behaviour of granular materials. The main advantage of this method is the generation of abundant information at the particle scale, which can be used to comprehend the physics of granular systems. This method is proven to be a comprehensive method to study granular soils [16, 17, 18, 19, 20, 21, 22, 23, 24]. The framework of this method is based on both contact law and motion equation. Contact model is applied to compute contact forces including normal and shear form from imposed contact deformations through the normal and shear contact stiffnesses, while motion equation is used to calculate the particle movement. In this paper, the DEM simulations are implemented using the software PFC^{2D} 4.1.

2.1. Contact law

The contact force ($\boldsymbol{F_i}$) applied on a disk particle in PFC^{2D} code is decomposed into normal force ($\boldsymbol{F_i^n}$) **and** tangential force ($\boldsymbol{F_i^s}$). The former is directed along the tangent to the particle and the latter is directed toward the particle center.

$$\boldsymbol{F_i = F_i^n + F_i^s} \qquad \textbf{(1)}$$

To preserve the geometry of particles during loading, it is assumed in PFC^{2D} that particles are rigid with soft contact, which means that a contact overlap between two particles (e.g., a and b) is applied rather

than a contact deformation. The magnitude of this overlap is computed by a contact law. In the present study, a linear elastic contact law is applied to calculate the components of contact forces. The normal and tangential displacements at time step $\boldsymbol{\Delta_t}$ is calculated as follows:

$$\boldsymbol{\Delta_n} = [(\dot{\mathrm{x}}^b - \dot{\mathrm{x}}^a)]\,\boldsymbol{n}\,\Delta_t$$
$$\boldsymbol{\Delta_s} = \left\{[(\dot{\mathrm{x}}^b - \dot{\mathrm{x}}^a)]\boldsymbol{t} - \left(\dot{\theta}^a|R^a| + \dot{\theta}^b R^b\right)\right\}\Delta_{\boldsymbol{t}} \quad \textbf{(2)}$$

where $\dot{\mathrm{x}}^a$, $\dot{\mathrm{x}}^b$, $\dot{\theta}^a$ and $\dot{\theta}^b$ are translational and rotational particle velocities of particle a and b, respectively. R^a and $R^b$are the particle radius. $\boldsymbol{n}$ and $\boldsymbol{t}$ are the normal and tangential unit vector of.

To calculate inter-particle normal force, contact models including linear elastic or Hertzian [25] can be used. In the present study, a linear elastic model is applied. The magnitude of the normal and tangential contact forces is calculated via:

$$(\boldsymbol{F_i^n})_{\boldsymbol{t}} = (\boldsymbol{F_i^n})_{\boldsymbol{t-1}} + (\Delta \boldsymbol{F_t^n})_{\boldsymbol{t}} \quad \text{where } \Delta \boldsymbol{F_t^n} = K_n(\boldsymbol{\Delta_n})_{\boldsymbol{t}} \quad \textbf{(3)}$$

$$(\boldsymbol{F_i^s})_{\boldsymbol{t}} = (\boldsymbol{F_i^s})_{\boldsymbol{t-1}} + (\Delta \boldsymbol{F_i^s})_{\boldsymbol{t}} < \mu(\boldsymbol{F_i^n})_{\boldsymbol{t}} \text{ where } \Delta \boldsymbol{F_t^s} = K_s(\boldsymbol{\Delta_s})_{\boldsymbol{t}} \quad \textbf{(4)}$$

The total contact shear force is compared to the Coulomb sliding friction or sliding capacity criterion (i.e. $\mu(\boldsymbol{F_i^n})_{\boldsymbol{t}}$) to check whether sliding has occurred. When the resultant force and torque in the z-direction (calculated by multiplying tangential contact force by the distance from the particle center to the contact location) are computed for each particle, the local damping force $\boldsymbol{F_i^d}$ will be added to them:

$$\boldsymbol{F} = \sum[(\boldsymbol{F_i^n})_{\mathrm{t}}\boldsymbol{n} + (\boldsymbol{F_i^s})_{\mathrm{t}}\boldsymbol{t}] + \boldsymbol{F_i^d}$$
$$\boldsymbol{M} = \left[\mathrm{R}\sum[(\boldsymbol{F_i^s})_{\mathrm{t}}\boldsymbol{t}\right] + \boldsymbol{F_i^d} \quad \textbf{(5)}$$
$$\boldsymbol{F_i^d} = -\alpha|\boldsymbol{F}|sign(\dot{x}); \qquad sign(v) = \begin{cases} +1, & \text{if } \dot{x} > 0 \\ -1, & \text{if } \dot{x} < 0 \\ 0, & \text{if } \dot{x} = 0 \end{cases}$$

where $\boldsymbol{\alpha}$, $|\boldsymbol{F}|$ and $\dot{\boldsymbol{x}}$ are damping constant, resultant force on the particle and particle velocity, respectively. The computed resultant force and torque acting on the particle is used to determine the change in particle velocity via Newton`s second law for the next time step.

3. Soil Fabric

In granular mechanics, soil fabric refers to the size, shape and arrangement of soil particles. Fabric quantities include either particle orientation, if 2D disk particles are used, or contact orientation and branch vector orientation for non-circular particles. These fabric quantities are often presented as an average or graphically (e.g. polar diagram of contacts). Rothenburg et al. [26] proposed a closed form solution to estimate the polar diagram of contacts.

$$E(\theta) = \frac{1}{2\pi}[1 + a\cos 2(\theta - \theta_a)] \quad \textbf{(6)}$$

where a represents "fabric anisotropy" in a granular system, depending on the number and density of unit normal vectors in principles axes. Note, Equation (6) should be drawn in polar coordinates. The shape of $E(\theta)$'s function is circular in polar coordinates and $E(\theta)$ represents mathematically the radius of the polar diagram distribution of normal contacts at each θ value. The variable θ, which is measured

clockwise, varies between 0° and 360°). Figure 1 schematically illustrates the concept of $E(\theta)$ and θ. a represents the deviation between the geometry of contact distribution and the isotropic contact distribution. For example, if $a = 0$, $E(\theta)$ will be a circle such that the state of the system being considered is in an isotropic state. θ_a *is* the direction of anisotropy. Parameters, a *and* θ_a, are obtained by the following equations:

$$a = \frac{2\sin\Delta\theta}{N\Delta\theta}\sqrt{\left[\sum_{g=1}^{n_g} N_g \sin\left((2g-1)\Delta\theta\right]^2 + \left[\sum_{g=1}^{n_g} N_g \cos\left((2g-1)\Delta\theta\right]^2\right.} \quad \textbf{(7)}$$

$$\theta_a = \frac{1}{2}\tan^{-1}\frac{\sum_{g=1}^{n_g} N_g \sin((2g-1)\Delta\theta}{\sum_{g=1}^{n_g} N_g \cos((2g-1)\Delta\theta} \quad \textbf{(8)}$$

where N is the total number of contacts, $\Delta\theta = \frac{360}{n_g}$, $n_g$the number of segments and N_g is the number of contacts within the g^{th} segment. Figure 1 schematically presents the concept of segment, n_g, highlighted in Equation 7 and Equation 8.

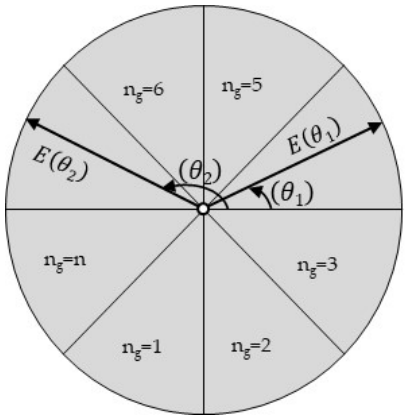

Figure 1 Schematically presentation of the concept of $\boldsymbol{E(\theta)}$, $\boldsymbol{\theta}$, segment, $\boldsymbol{n_g}$highlighted in Equation 6 to Equation 8

In fact, fabric anisotropy parameter shows the ability of granular systems to create the anisotropy state in normal contact distribution. Rothenburg [27] applied a similar idea to estimate an analytical form of polar diagram for normal contact force distribution, $\bar{f}_n^c(\theta)$, of an idealised 2D particulate system during loading:

$$\bar{f}_n^c(\theta) = \bar{f}_0^c[1 + a_n \cos 2(\theta - \theta_n)] \quad \textbf{(9)}$$

where a_n is the normal contact force anisotropy. Note, similar to Equation (6) the above Equation should be drawn in polar coordinates. θ_n is a direction of $\bar{\boldsymbol{f}}_{\boldsymbol{n}}^{\boldsymbol{c}}(\boldsymbol{\theta})$. The similar approach applied to specify a_n and θ_n:

$$\bar{f}_0^c = \frac{1}{2\pi}\sum_{g=1}^{n_g} f_n^c(g)\Delta\theta \quad \textbf{(10)}$$

$$f_n^c(g) = \sum_{i=1}^{nc_g} f_n^{c_i}$$

$$a_n \sin 2\theta_n = \frac{1}{\pi \bar{f}_0^c} \sum_{g=1}^{n_g} f_n^c(g) \sin((2g-1)\Delta\theta)\Delta\theta$$

$$a_n \cos 2\theta_n = \frac{1}{\pi \bar{f}_0^c} \sum_{g=1}^{n_g} f_n^c(g) \cos((2g-1)\Delta\theta)\Delta\theta$$

where nc_g and $f_n^{c_i}$ are the number of contacts within g^{th} segment and the normal contact force of i^{th} contact from g^{th} segment respectively. If $a_n = 0$, $\bar{f}_n^c(\theta) = \bar{f}_0^c$. That is, the system is likely to be isotropic [22]. One of the key microscopic parameters, which are defined at particle-level, is the average coordination number which increases with densification [28, 29]. This parameter is the average number of contacts per particle within a specific volume of a particulate assembly and consequently it provides a measure of packing density or packing intensity of fabric at particle-level. For a volume of particulate assembly with N_p particles and total number of contacts, N_c, the definition of average coordination number C_n is given by:

$$C_n = \frac{2N_c}{N_p} \quad \textbf{(11)}$$

Since each contact is shared between two particles, the actual number of contacts is multiplied by 2. Rothenburg and Kruyt [30] and Maeda [31] have shown that average coordination number should be at least three for idealized disk particle when a granular system is in quasi-static equilibrium.

4. Geometrical stability index

The fabric quantities illustrated above are average quantities for a volume of particles. For instance, the average coordination number provides an average measure of bulk packing density. However, this average fabric quantity cannot demonstrate how contacts are distributed around a particle. This issue was considered in average normal contact distribution which statistically describes the orientation of contacts during loading. These collective fabric terms can be used to interpret the bulk stability of a granular system and give an indication of the response and bulk instability [9, 28]. However, instability occurs at a particle level which may progress causing local instability. Geometrical stability index, ʎ, is a state-of-the-art fabric term which can measure the contact deviation of each particle from the arrangement of the most stable contacts during loading [32]. In this concept, a set of n-stable contact arrangements is defined for each particle which is in contact with n particles. The radial distance between two contacts on the perimeter of a particle is the minimal angle between them. The deviation of the contact arrangement of a particle, d^{Sn}, from a geometrical stable contacts arrangement is expressed as the sum of the deviation of each contact point, $d(s_i^n)$, from the associated stable location such that:

$$d^{Sn} = \sum_{i=1}^{n} d(S_i^n) \quad (12)$$

This is repeated for each contact. The minimum value of d^{Sn} is D:

$$D = \min\{d^{Sn}\} \quad (13)$$

To make it dimensionless, it is divided by 360°.

$$\lambda = \frac{D_M}{360} \tag{14}$$

in which λ is geometrical stability index.

Figure 2a shows particle, D, is contact with three particles, A, B and C. A set of 3-stable contact arrangements is defined for this contact arrangement as shown in **Figure 2**b–d. If the angle between particle A and particle B is 120 ° and the angle between particle B and particle C is 120 °, there is geometric stability. If either of these angles ≠ 120 ° then the configuration is no longer geometrically stable. This is expressed in terms of the deviation of the lines connecting the centers of the particles from the geometrically stable configuration. The dash lines in each of these figures is the stable contact configuration, when the angle between them is 120 °.

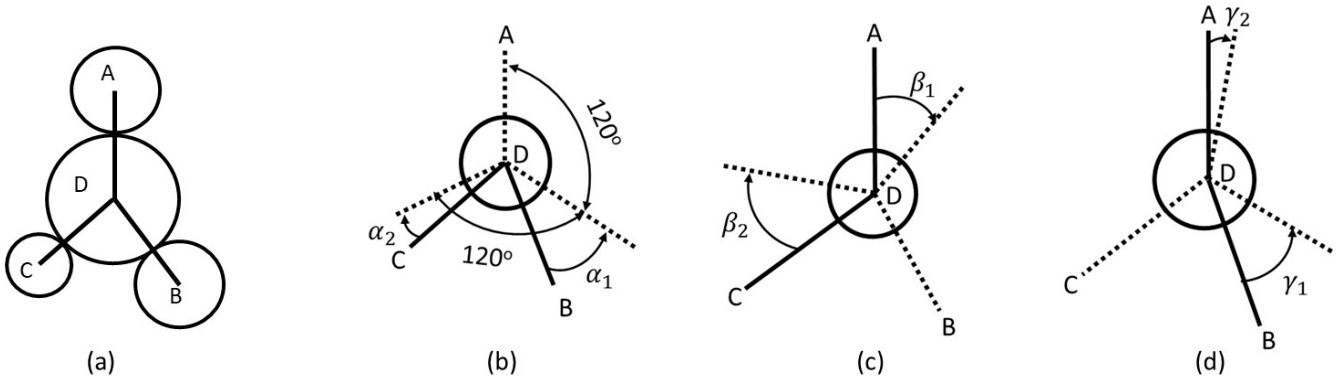

Figure 2 Concept of geometrical stability index (After Momeni et al. 2022 [])Therefore, there are three sets of d^{Sn}. For the first set (Figure 2b):

$$d^{Sn^A} = \alpha_1 + \alpha_2 \tag{15}$$

For the second set (Figure 2c)

$$d^{Sn^B} = \beta_1 + \beta_2 \tag{16}$$

For the third set (Figure 2d):

$$d^{Sn^C} = \gamma_1 + \gamma_2 \tag{17}$$

Thus, the geometrical stability index for this particle is:

$$\lambda_2 = \frac{min\{d^{Sn^A}, d^{Sn^B}, d^{Sn^C}\}}{360} \tag{18}$$

It is assumed that particles with one or no contact are not stable and are assigned a value of λ of one. Reader to refer to Momeni et. al [32] for more details of this state-of-the-art fabric term.

5. Boundary conditions in DEM biaxial test overview

In this paper, two-dimensional biaxial specimens consisting of 2D idealized disk particles are used to qualitatively investigate the sensitivity of the micro-macro mechanical behaviour of idealized granular sand to the side boundary conditions: rigid boundary and deformable boundary. Particles are initially generated within a chamber enclosed with four rigid boundaries then isotropically consolidated to the target confining pressure. As biaxial specimen is sheard, the confining stress along the side boundaries is maintained at a constant value in combination with a servo-controlled system to control the stress. A servo-control mechanism together with boundary conditions are required to be employed in DEM biaxial tests to maintain the hydrostatic confining pressure during application of the deviatoric load.

The servo-control is used at the side boundaries of the sample. A rigid boundary is usually employed by DEM analysts [32, 33, 34]. In this approach, a specific velocity is given to the rigid boundary through the servo-control to maintain the target confining pressure. However, the true fabric evolution and bulk deformation of sample cannot be developed as the rigid boundaries inhabit the free movement of boundary particles. Additionally, the magnitude of contact forces developed between those particles that are in contact with the rigid boundary are high. This results in significant changes in the macro stress distribution over the boundary. Using an inflexible boundary takes longer for the particulate sand system to reach the critical behaviour. As stated by Momeni [32] the elastic parameters including Young's modulus and Poisson's ratio attained from inflexible boundary can be reliable. To show a true bulk deformation (e.g. bulge deformation and true shear band) and fabric evolution a deformable boundary should however be employed. Similar to continuum model where boundary conditions can be either displacement or force control over the nodes of boundary elements, the boundary condition in a DEM simulation can be expressed by either displacement or force control over the boundary particles. The concept of displacement boundary condition is to maintain the confining stress over each boundary particle, in two directions, σ_x and σ_y, to a target stress value by adjusting the velocity of each boundary particle in two directions, $\dot{\mathbf{u}}_\mathbf{x}$ and $\dot{\mathbf{u}}_\mathbf{y}$, within a biaxial sample. At the start of each time step, the value of the boundary particle stresses within the biaxial chamber in two directions, σ_x and σ_y, is calculated by DEM solver (e.g. PFC^{2D}) and compared with the target confining stress, σ_t. If the boundary particle stresses are equal to σ_t, the particle velocity, $\dot{\mathbf{u}}_\mathbf{x}$ and $\dot{\mathbf{u}}_\mathbf{y}$ will be set to zero; otherwise the particle velocity might be adjusted through the following relation:

$$\dot{\mathbf{u}}_\mathbf{x} = \mathrm{G_x}(\boldsymbol{\sigma}_\mathbf{x} - \boldsymbol{\sigma}_\mathbf{t}) \quad \text{where} \quad \mathrm{G_x} \le \frac{\beta\, \mathrm{A_x}}{K_n \Delta t}$$
$$\dot{\mathbf{u}}_\mathbf{y} = \mathrm{G_y}(\boldsymbol{\sigma}_\mathbf{y} - \boldsymbol{\sigma}_\mathbf{t}) \quad \text{where} \quad \mathrm{G_y} \le \frac{\beta\, \mathrm{A}_y}{K_n \Delta t} \tag{19}$$

where $\mathrm{G_x}$, $\mathrm{G_y}$, $\mathrm{A_x}$, $\mathrm{A_y}$, β, $\mathrm{K_n}$ and Δ_t are the gain parameter, projection area of particle in x and y directions, a constant value between 1 and 0.01, normal contact stiffness and time step. The projection area of particle in x and y directions will be explained in Section 6.1. A change in the displacement value given to a boundary particle leads to a change in its deformation value with neighboring particles. This alteration in the contact deformation of a boundary particle results in a change in its contact force value and stress value. For stability, the absolute value of the change in particle stresses must be less than the absolute value of the difference between the measured and target stresses. This prevents overshooting of the target stress, which would lead to an oscillation about the target stress that would grow in an unbounded fashion and lead to numerical instability.

In the force boundary condition, an external force equal to the target confining stress applied to the boundary particles at each time step to maintain the target confining stress. However, using force boundary conditions is more efficient since in displacement boundary conditions at each time step the stress tensor of each boundary particle should be calculated and compared with target confining stress. Periodic boundary is also used by DEM analysts to simulate the boundary of DEM models [35, 36]. In this approach, the particulate element is virtually extended in all directions by repeating this element. Additionally, either displacement or force boundary conditions should be coupled over the periodic boundary particles to maintain the target confining stress during the biaxial test. The use of periodic boundaries has the following effect on the physics of the DEM model. When a particle flies over the periodic boundary, a new particle with the same properties enters the system from the adjacent virtual system on the opposite side. When this boundary condition is applied, the expansion and localization of the model during loading cannot be take place because the dimension of periodic space is already set to a constant value. When the system expands, the displacement of boundary particles may exceed the set periodic space. At this stage, those boundary particles will be removed automatically, and the same

particle enters the system from the adjacent virtual system on the opposite side. This leads to change in the normal shear force distribution on the boundary. However, any unexpected changes in boundary particles result in change in the average un-balanced force system. That means the significant and permanent chaos in un-balanced forces and particle velocities will be take place. Thus, the magnitude of deviatoric load should be small enough to prevent boundary particles passing the periodic boundary. El Shamy and Denissen [37] applied periodic boundary to investigate liquefaction phenomena using DEM simulations. Zamani and El Shamy [38] studied earthquake seismic wave propagation through the dry granular soil using PFC^{3D} [39] qualitatively. The periodic boundary condition was used for this work.

6. The history of simulating membrane latex in DEM

The role of latex in triaxial test is to prevent the pressurized fluid getting into the sample, allowing the system to naturally deform during loading. To simulate this in DEM, those particles that are in contact with latex in the real triaxial text should be identified through the given algorithm. These boundary particles should also behave similarly to the latex membrane in a real physical test. Two algorithms are generally applied to identify the boundary particles by DEM analysts. In both algorithms the sample enclosed with rigid boundaries is firstly isotropically consolidated. People including [8, 9, 10, 13, 40] first identified those particles are in contact with rigid side boundaries. They then applied a contact bond with a high tensile capacity between the boundary particles. The boundary particles in this method cannot be updated as the boundary particles are bonded initially. Additionally, the magnitude of the contact bond should be high enough to not fail during bulk expansion. As the moment stiffness of latex applied in triaxial tests is ignorable, bonding the lateral boundary particles generates larger moment stiffness than recommendable to model experiments properly. Therefore, boundary particles cannot freely move during loading. This difficulty was sorted out partially in the work carried out by Cheung and O'Sullivan [41] who developed an algorithm written by FISH language programming to simulate a lateral membrane boundary for biaxial test using PFC^{2D}. They applied force control boundary conditions to maintain the confining stress along the boundary particles. In this approach, frictionless membrane particles can deform freely during testing without bounding them, while maintaining a specified stress condition. O'Donovan et al. [42] applied this algorithm to maintain confining pressure over the lateral boundaries in order to study two-dimensional seismic S-waves propagation within an idealized frictional uniformly-radius sized disks 0.0029 [m] in a hexagonal packing using a series of PFC^{2D} simulations. At large deformation where the biaxial specimen starts to bulge or a shear band traverses the sample, a number of particles that have been already part of membrane boundary particles may separate from the biaxial sample by losing their contact with other particles within the sample. Based on this algorithm, those particles that have been separated from the specimen and flown over the boundary are identified by only comparing the x-coordinate of each particle centroid within the specimen with the minimum centroidal x-coordinate of the boundary particles. As the membrane boundary deforms during loading, both y- and x-coordinates of separating particles need to be considered to identify escaping particles from boundary. This will help to insert these particles to an appropriate position at the boundary, which was not clear from the work of Cheung and O'Sullivan [41] and O'Donovan et al. [42]. In the current paper we introduce a slightly modified algorithm to simulate the continuous latex membrane for biaxial test simulation using PFC^{2D}. This algorithm is described in detail below.

6.1. Deformable lateral boundary

This section will explain the algorithm to produce deformable lateral boundaries. When the two-dimensional granular system enclosed with four rigid boundaries is isotropically consolidated, the two lateral boundaries are removed and two deformable membrane lateral boundaries are applied to

maintain the lateral confining stress. For this purpose, comprehensive subroutines using PFC^{2D} and fish language programming [15] were developed to derive the pathway of deformable boundary particles. The stages of this algorithm which is based on directed graph theory is as follows:

1. Introduce two separate ranges for the left- and right-hand sides of the sample to recognize the boundary particles (see **Figure 3**(a)). The boundary particles should form two continuous chains at the edge of the model. This means that the centroid of particle (i) is above the centroid of particle ($i-1$) and below the centroid of particle ($i+1$). However, this is not always the case as shown in **Figure 3**(b) where some particles at the edge of the model are not part of the chain, i.e. while particles in Figure 3b. This means that the deformable boundary lies within a boundary zone. Trial and error study showed that the zone was ten times the mean particle size.

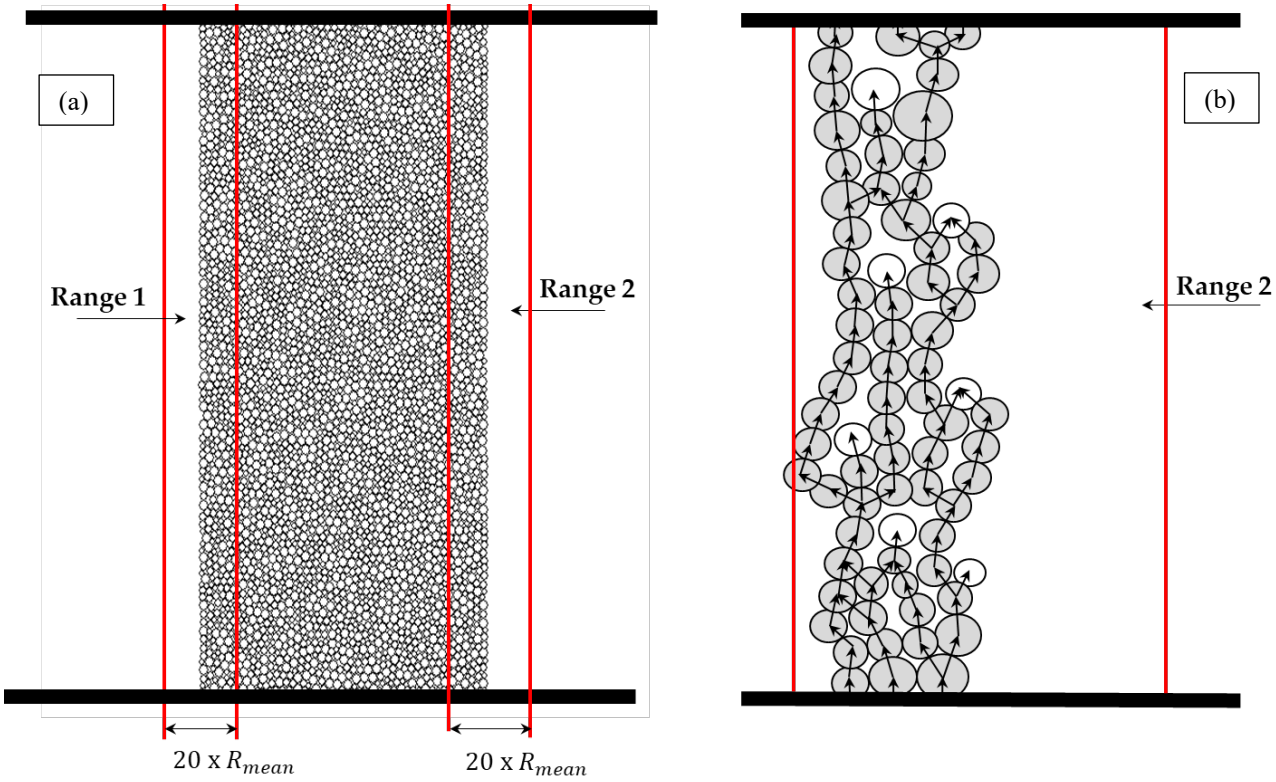

Figure 3 (a) Define two separate ranges for left- and right-hand side of the sample. (b) Finding the degenerate particles on left boundary schematically

2. Two-dimensional arrays are then defined to store all the particles' addresses within the ranges stated in stage 1. The first component of array is to store the particles' identification (i.e. particle number and the second component of array is to assign an index "1" or "0" to all these particles, executed in the next stage.

3. A loop upon all particles stored in arrays, defined in stage two, are executed and the index of the particles are assigned to "1" and "0" for particles that are in contact with their immediate above and those that are not in contact with their immediate above particle, respectively. These are shown in Figure 4a (gray and while particles assigned with the index of 1 and 0, respectively).

4. Next, the loop will be continued to find the degenerate directed graphs (white pathway in **Figure 4**(a)) and continuous directed graphs (light gray pathways in **Figure 4**(a)).

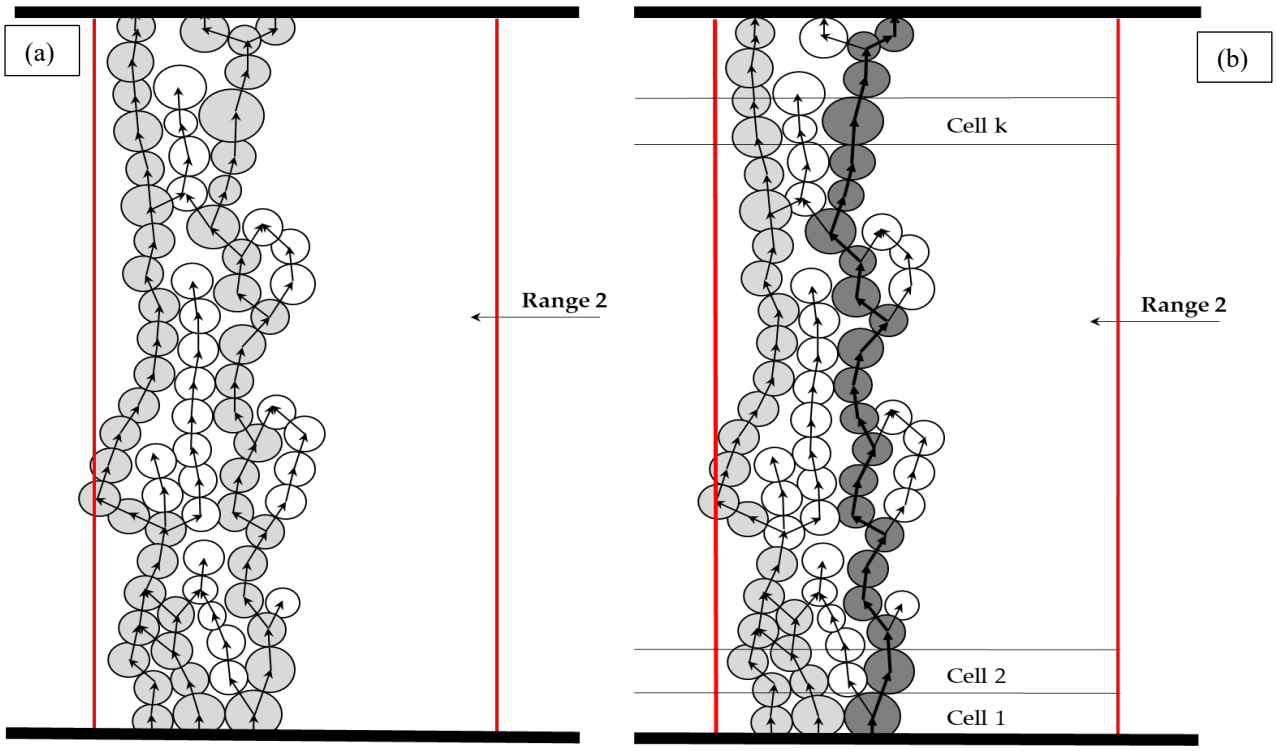

Figure 4 (a) Determination of all degenerate particles and paths within Range 2 (right range) schematically, (b) Determination of boundary particles

5. Next, the non-degenerate outermost right-hand particle which is in contact with the bottom wall is recognized. The outermost right dark gray pathway shown in **Figure 4**(b) is then selected as deformable boundary particles because the connectivity between them leads to transmit properly the hydrostatic pressure to the sample.

6. During shearing of the biaxial specimen where the sample experiences large deformation, some particles separate from the specimen and pass the boundary. A separate cell is assigned to each individual deformable boundary particle which was identified in stage 5. The cell number, y-coordinate of the bottom and top of each cell and x-coordinate of deformable boundary particle centroid are stored in a four-dimensional array. To recognize those particles separating from the specimen and passing over the deformable boundary particles the following stages need to be implemented:

- Comparing the y-coordinate of all particles within the right range with the bottom and top y-coordinates of right cells, defined in the array above, to identify the cell number which can be allocated to each particle.

- Comparing the x-coordinate of all particles with the x-coordinate of their corresponding cell number, defined in the array above,

- If the x-coordinate of particle is greater than the x-coordinate of its corresponding cell, that particle is marked as a particle outside the boundary. For the left deformable boundary, if the x-coordinate of particle is less than the x-coordinate of its corresponding cell, that particle is marked as a particle outside the boundary.

7. The inter particle friction of the boundary particles is set to zero because it is assumed that these particles form the interface between the external pressure and the soil model and only transmit lateral pressure. In practice, latex is used which is considered a frictionless material [36].

8. While in practice a uniform pressure is applied, in the DEM model a force is applied to each boundary particle. The force divided by the effective length is equal to the confining pressure, σ(t), (see **Figure 5**(a)). The effective length is defined by the line connecting the two contact points which defines the pathway through the particle (see **Figure 5**(b)). The magnitude of this force for each deformable boundary particle is σ(t) × effective length. The components of the boundary forces are the product of the external pressure and the effective length (see **Figure 5**(c)).

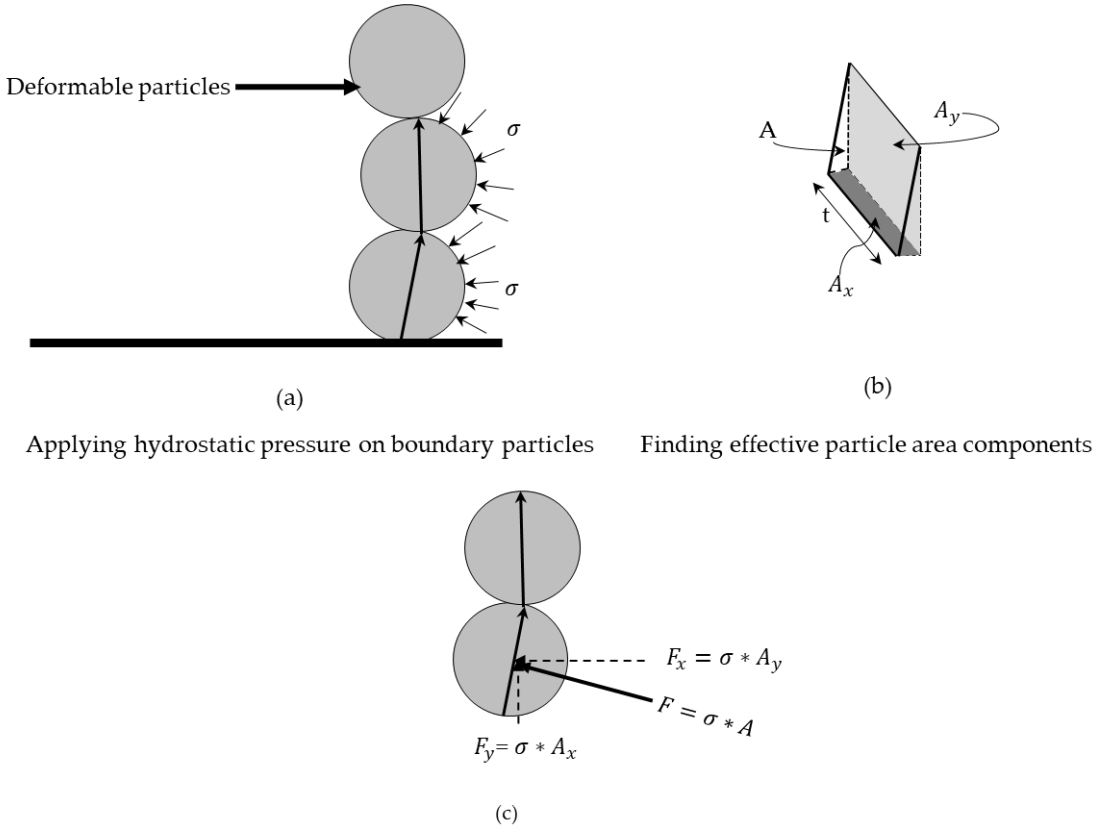

Figure 5 Applying external forces on right boundary particles schematically.

9. As the deviatoric loading proceeds, some particles near the edge of boundary (white particles in Figure 4b) may fall outside the boundary by losing their contact with deformable boundary particles. Once a particle is passed the deformable boundary, a force equal to the σ(t) × particle diameter is then applied to push them back to the deformable boundary particles in the following time step. This resembles holding particles using latex with lateral confining pressure (σ_t) in real experiments where each particle at the edge of boundary faces the aforementioned pressure, pushing it back to the assembly. The process to identify the boundary particles is repeated.

10. The same procedure is applied for the left boundary particles.

11. Stages three to nine are invoked every time step.

The advantages of this approach over those mentioned before is that the boundary particles are always in real contact though the actual particles forming the boundary may change between time steps. At larger displacements where the biaxial sample is sheared, there is a possibility that the formed particle chain at the boundary changes in each time step, introducing instantaneous changes in the positions in which the boundary is considered during the application of the lateral pressure to the system.

6.2. The sensitivity of micro-macro mechanical behaviour of particulate system to the lateral boundary conditions

To study the influence of boundary conditions on the micro-macro mechanical behaviour of particulate sand, two biaxial tests were performed. One test was with deformable boundary particles and other was with a rigid wall boundary. To avoid overlapping at the generation stage, disk particles with the size range of 0.5 [mm] and 3 [mm], corresponding to a well graded sand, were initially randomly generated with their half size (i.e. 0.25 [mm] and 1.5 [mm]) within four enclosed rigid walls. Ideally, there should be at least three contacts per idealised disk particle (i.e. the average coordination number) when a granular system is in quasi-static equilibrium. By doing this, the chains' force can transmit across the particulate system. For this purpose, the half-sized generated particles in the biaxial chamber were expanded to achieve the different target porosity of 0.08, 0.09, 0.1, 0.11, 0.12, 0.13, 0.14, 0.15, 0.16 and 0.17. It was observed that the samples with target porosity between 0.12 and 0.14 can produce at least three contacts per particle, therefore porosity of 0.12 was chosen for this study. Linear elastic contact model was used in this study. It is to be noted that the inter-particle properties for typical sand used for this study was selected based on the sensitivity of micro-macro mechanical behaviour of sand to the inter-particle properties by Momeni et. al [44]. They conducted thirty DEM biaxial tests to study the sensitivity of the macro-micro mechanical properties of particles to the inter-particle properties of an idealized sand system. Their research identifies the critical parameters and the range over which the parameters impact mass behaviour. The time step required to simulate the biaxial test must be very small to prevent instability of the model. The density scaling approach, originally developed by Sheng et al. [43], was applied in this work to increase the time step and decrease the computational effort of simulations. A dimensionless inertia parameter, I, was introduced to study the effect of density scaling for various strain rates applied to the particulate systems. This method is only applicable for quasi-static simulation where, I, in the following equation must be less than 10^{-3} [43].

$$I = \sqrt{\frac{\dot{\varepsilon}^2 \rho r_{min}^2}{p_y}} \quad \textbf{(20)}$$

where $\dot{\varepsilon}$, r_{min}, p_y and ρ are the strain rate, the minimum radius of the particles, the limiting contact pressure between particles and the density of the particles. There is a transition zone in the behaviour of the materials near $I = 10^{-3}$ for which higher values of I leads to a transient and dynamic behaviour, and the behaviour maintains a quasi-static response for lower values. A sensitivity analysis showed that the particle density $\rho = 2\text{x}10^8$ $[\frac{kg}{m^3}]$ can reproduce the similar macro-micro behaviour as real particle density $\rho = 2650$ $[\frac{kg}{m^3}]$. The particle size distribution is presented in **Figure 6**. **Table 1** shows the input data used for this study.

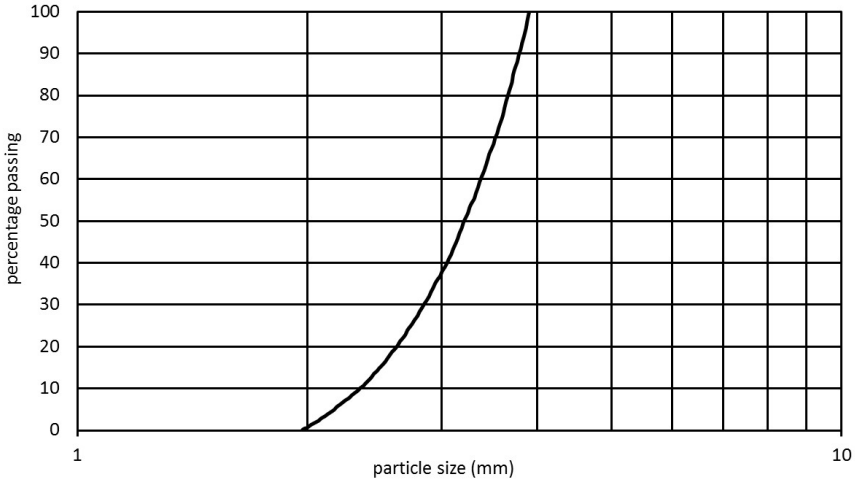

Figure 6 Particle size distribution

Initial porosity	0.12
Normal particle stiffness: K_n	8.45×10^7 [N/m]
D_{50}	1.7 [mm]
Shear particle stiffness: K_s	8.45×10^7 [N/m]
Coefficient of friction between particles	0.9
Coefficient of friction between a particle and the platen	0.0
Width	75 [mm]
Height	150 [mm]
Strain rate: $\dot{\varepsilon}$	2%/min
Particle density: ρ	2×10^8 [kg/m^3]
Contact pressure: p_y	150 [MPa]

Table 1 The initial porosity and micro-mechanical properties of the sample

Once the biaxial specimen reaches to the target porosity, the sample was isotropically consolidated to 100 [kPa]. Additional cycles were then executed to bring the system to a static equilibrium. From this point forward one test was carried out with rigid boundaries while applying servo-control mechanism to maintain lateral stress of 100 [kPa] during shearing of the sample (see Figure 7b). At the start of each time step, the average stress along the rigid lateral wall, $\sigma^{(w)}$, is calculated by summing the particle-wall contact force (f_c^{pw}) over the area of wall, A.

$$\sigma^{(w)} = \frac{\sum f_c^{pw}}{A} \tag{21}$$

The wall stress is then compared with the target stress. If the wall stress is equal to $\sigma^{(t)}$, the wall velocity will be set to zero; otherwise the wall velocity, $\dot{u}^{(w)}$, should be adjusted through the following relation:

$$\dot{u}^{(w)} = G\left(\sigma^{(w)} - \sigma^{(t)}\right) \quad \text{where} \quad G \leq \frac{0.5\text{A}}{K_n \Delta t} \tag{22}$$

For the other test, the algorithm described above was applied to form deformable lateral boundaries and control the lateral stress state replaced the rigid boundaries (see **Figure 7a**). The top and bottom platens are then moved slowly inward at a constant velocity to perform a strain-controlled test. The strain rate applied for these two tests was $\frac{2\%}{min}$ such that the incremental acceleration of each particle at each time step is small. All the imposed energy generated during the simulation was dissipated through frictional sliding between particles and loss of contacts. During the deformation of the sample, some boundary particles at the edge of the sample escape. The cell of these particles is then identified at the current time step. The coordinates of such particles are then not considered to calculate the volumetric strain and lateral strain until they touch the membrane boundary. These particles then push back to touch the membrane boundary by applying an external force to them. Once they touch the boundary, the applied external force on them will be removed.

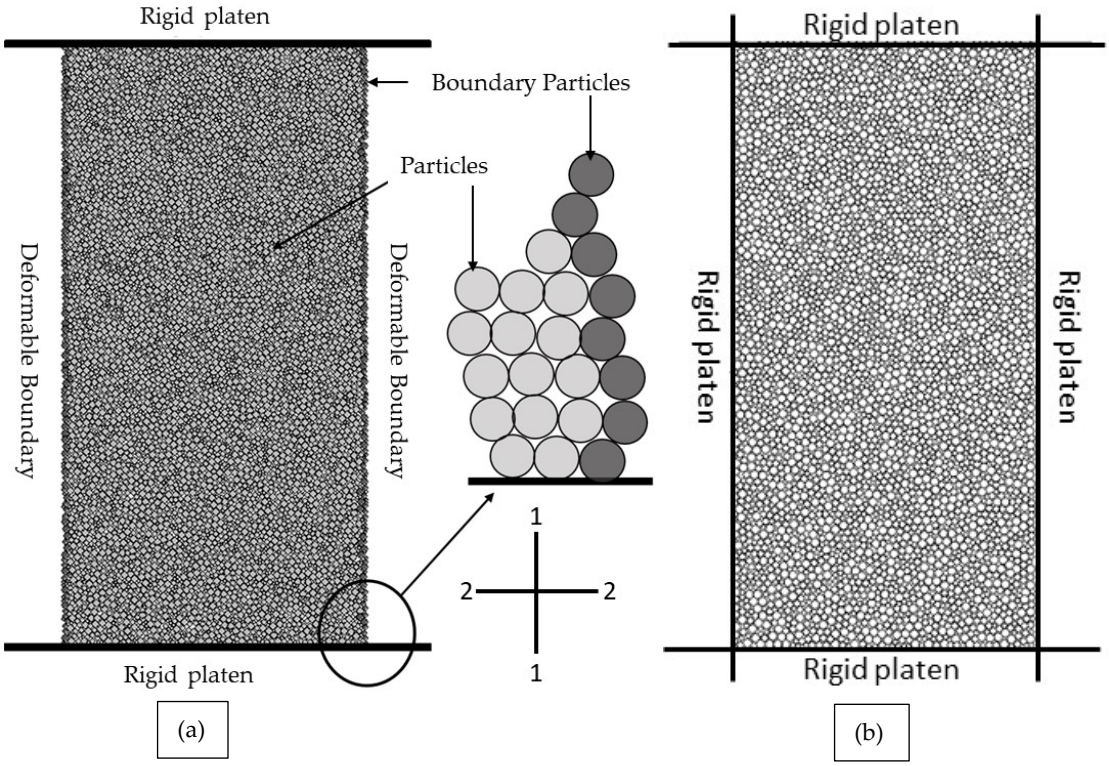

Figure 7 The biaxial sample: (a) deformable vertical boundaries, (b) rigid vertical boundaries; 1-1 and 2-2 are the direction of major and minor axis.

To precisely study the macro mechanical behaviour of granular soil, it is essential this system is investigated at a microscopic scale. To this end, fabric qualities of these two biaxial tests including average fabric anisotropy, average coordination number and average geometrical stability index with axial strain are considered. **Figure 8** compares the evolution of polar diagrams of contacts distribution of both samples during the shearing at three axial strain levels: at ε_{11}= 0.0% (i.e. at isotropic state), at axial strain corresponds to peak stress and at ε_{11}= 10%. To draw these polar diagrams, 18 bins were considered with an angular interval $\Delta\theta$ = 20°. The radius of each bin corresponds to the number of contacts. If the polar diagram is fully circled, it shows that the contact distribution is in an isotropic state. At ε_{11}= 0.0%, where both samples at macro-scale are isotropically consolidated to 100 [kPa], the average fabric anisotropy is 0.0034 and a circle can present the analytical contact distribution. The number of contacts per each segment is distributed almost equally. By applying a deviatoric load, the

contacts are aligned in the direction of major principal stress (i.e. 1-1 axis) to take the load. Note, the direction of major principal stress (axis 1-1) is in the same direction as the deviatoric stress. The average fabric anisotropy then rises to 0.35 and 0.29 for rigid and deformable boundaries, respectively. This shows the sample enclosed with four rigid boundaries enables to mobilize more contacts to take more load. Quantitatively comparing the diameter of the two polar diagrams at peak stress shows that the diameter of polar diagram for deformable boundaries is around 3200, while it is about 3600 for rigid boundaries. At ε_{11}= 10%, the orientation of contact points is toward the confining stress and average fabric anisotropy reduced to 0.27 and 0.18 for rigid and deformable boundaries. This indicates both systems are not able to mobilize more contacts after peak stress, meaning the particulate system has been collapsed.

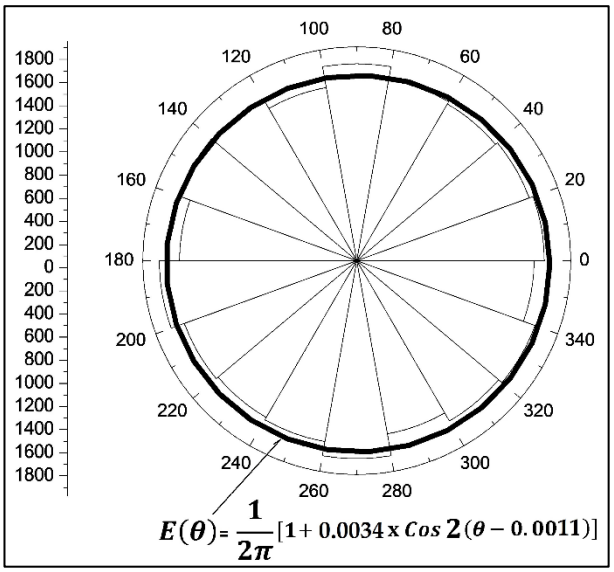

At ε_{11}= 0.0

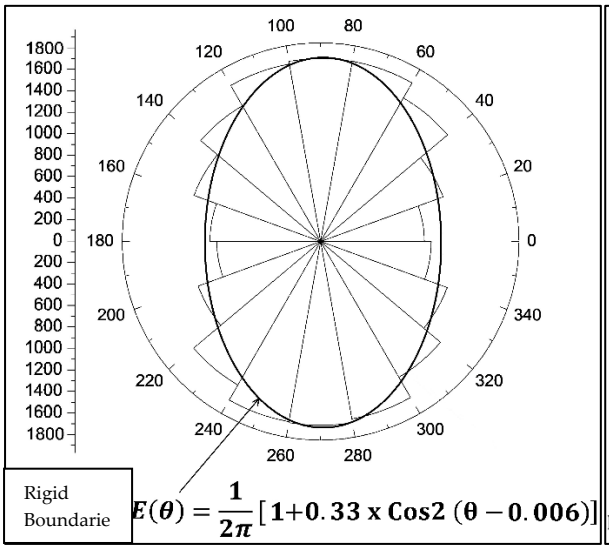

At peak stress

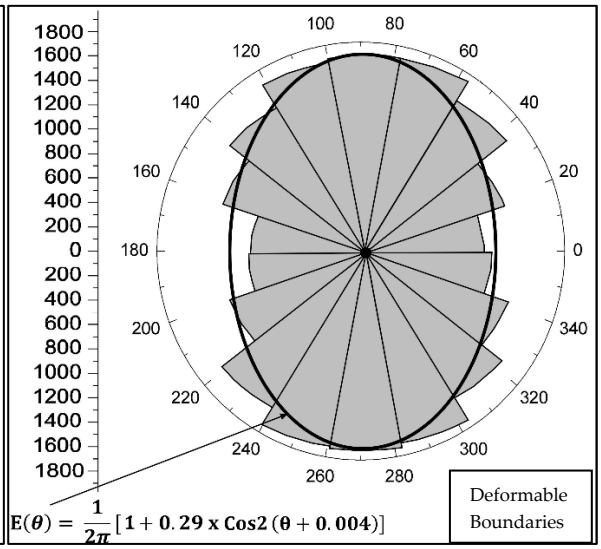

At peak stress

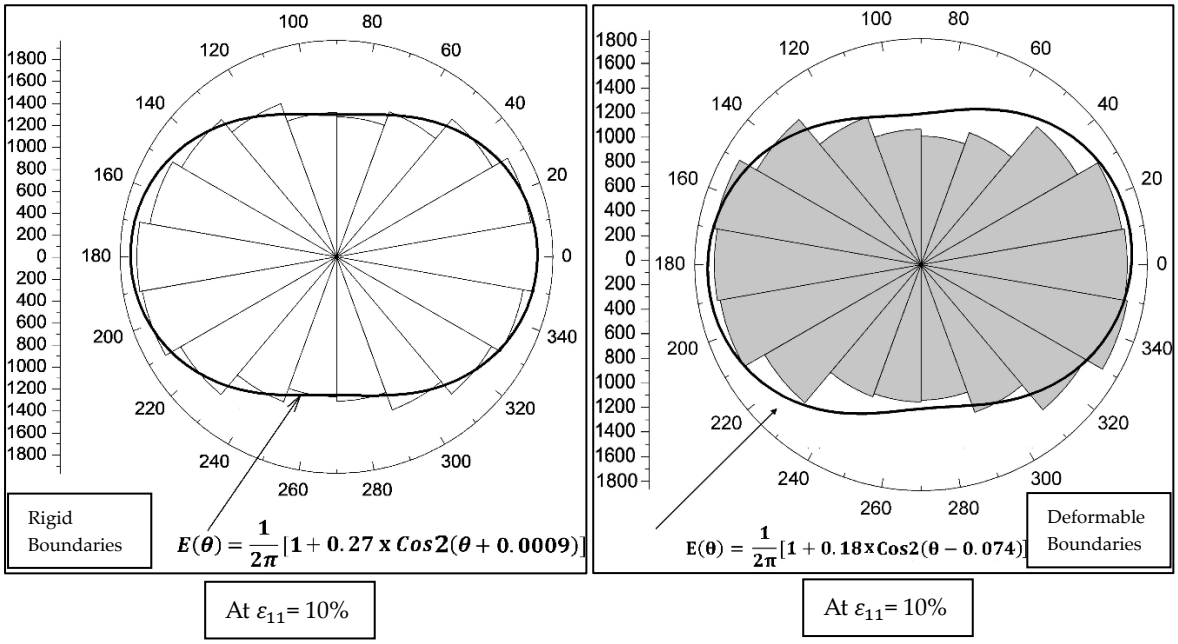

Figure 8 The evolution of contact distribution of particulate: rigid boundaries, deformable boundaries. Note, the unit of radial angle is "Degrees" and the unit of the radius of the polar diagram is "Number of contacts".

Figure 9a compares the variation of average fabric anisotropy vs. axial stain for the rigid and deformable boundaries. Up to an axial strain of about 1%, both simulations present a similar trend. From axial strain of 1% to 1.5%, the peak value of fabric anisotropy for rigid boundaries is more than that for deformable boundaries. The rigid lateral boundaries restrict the shape of lateral deformation and do not allow the particles to move freely. In contrast, particles along the deformable boundaries are free to move during shearing. For the deformable boundaries, the post-peak variation of fabric anisotropy (from the axial strain of about 4%) is less than that of the rigid, suggesting that the test with rigid boundaries probably requires longer time shear to reach the critical state. **Figure 9**b illustrates the variation of average coordination number against axial strain for different boundary conditions. The trend of average coordination number vs. axial strain between rigid boundaries and deformable boundaries is similar until peak fabric anisotropy. It is about 3.4 for rigid boundaries while it is about 3.0 for deformable boundary. The bigger the average coordination number, the more stable the granular system is. Therefore, the granular system enclosed with rigid boundaries has a bigger strength and is more stable than that with a deformable boundary. The trend remains relatively constant at 3.3 for the rigid boundaries, while it is about 2.9 for deformable boundaries. The reason of this decrease in average coordination number in the case of deformable boundaries after peak is its dilation behaviour. As the rate of dilation increases, the tendency of particles to move and lose their contacts increases and subsequently their stability decreases.

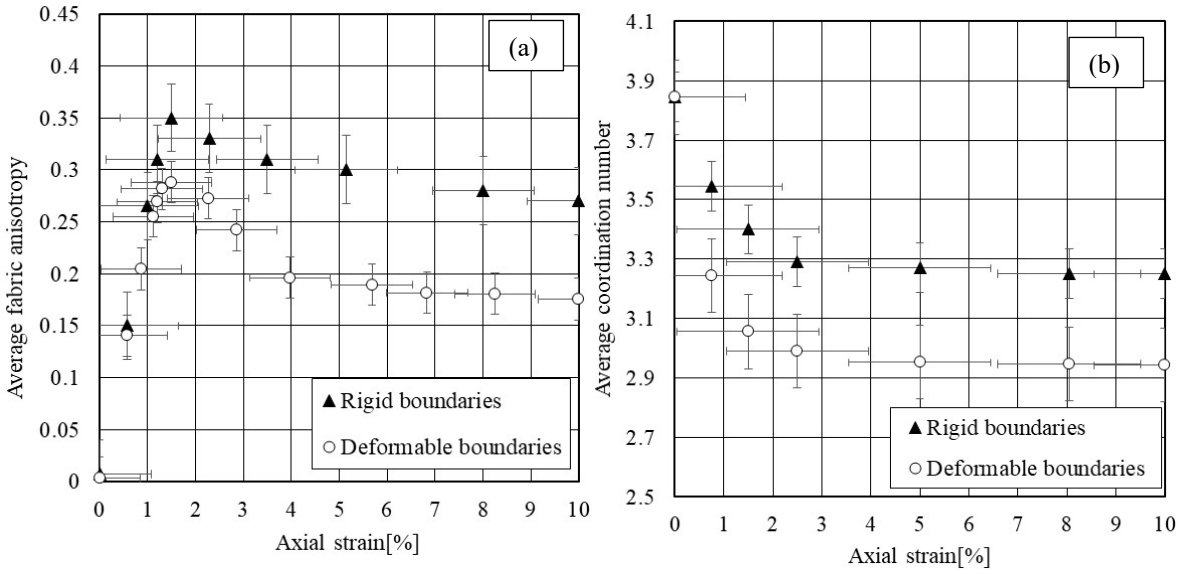

Figure 9 The sensitivity of (a) Average Fabric anisotropy and (b) average coordination number to the different boundary condition for rigid and deformable boundary

Applying the rigid lateral boundaries to maintain the confining pressures during shearing also results in a substantial increase in average normal contact forces, $\bar{f}_0^c$. For example, **Figure 10**a and **Figure 10**b compare the polar diagram and analytical form of normal contact force distributions for both deformable and rigid boundaries samples at the end of the test (i.e. $\boldsymbol{\varepsilon_{11}}$ = 10%). Similar to the polar diagram of contact distribution, 18 bins are taken into account with an angular interval Δθ = 20° to a draw polar diagram of normal contact force distribution. The radius of each bin corresponds to the summation of normal contact forces. The average normal contact forces, $\bar{f}_0^c$, at the end of the test are significantly different between these two models. As highlighted, the value of average contact forces is 160.82 [N] for the model using deformable boundaries, while it is 658.277 [N] for rigid boundaries. This notable discrepancy between these two values is because of the interaction between the rigid walls and the neighboring particles and the lack of free deformation at the lateral boundaries.

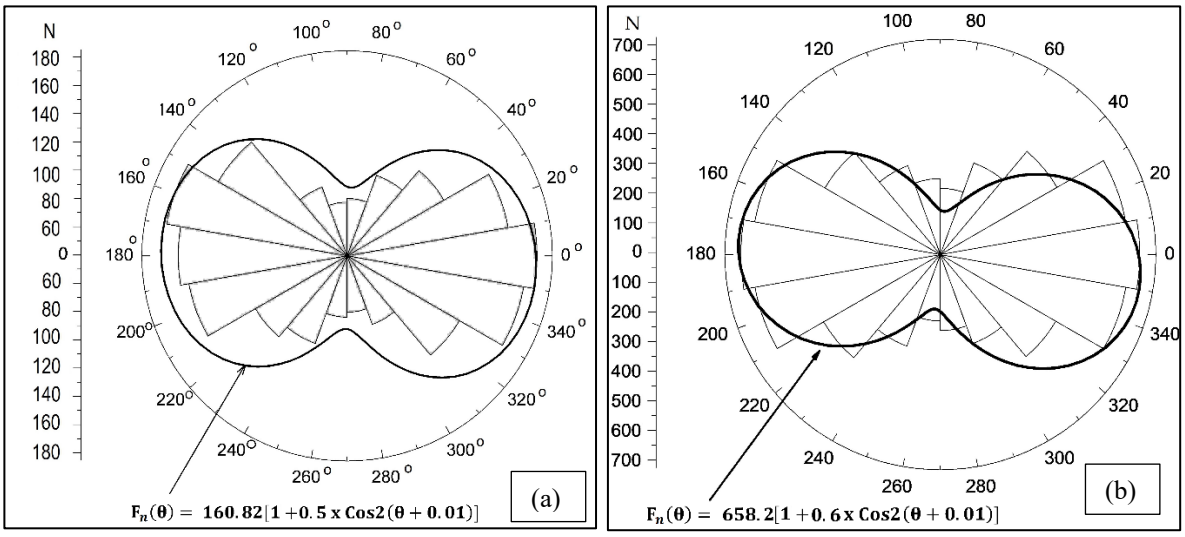

Figure 10 Normal contact force distribution at $\boldsymbol{\varepsilon_{11}}$ = 10% , (a) deformable boundary particles, (b) rigid boundary

The variations of average geometrical stability index for both samples are shown in **Figure 11**a. An equal distribution of contacts of an idealised 2D particle is defined as the most stable contact distribution

and the deviation of the contact distribution from the most stable contact distribution is the geometrical stability index. It is seen that when the samples are in an isotropic state, the average geometrical stability index is about 0.22. That means that the contacts around each idealised disk particle are not in a stable configuration. However, the value of this micro-scale descriptor increases for both samples during shearing. Up to an axial strain of about 1.5%, where the contacts are orientated toward the major principal stress and corresponds the peak fabric anisotropy and inflection point in average coordination number, the trend of average geometrical stability index significantly increases to around 0.33 and 0.35 for deformable boundaries and rigid boundaries, respectively. However, beyond this point this behaviour significantly diverged such that the trend for deformable boundary significant dropped to around 0.29 at an axial strain of about 4% and then slightly reduced to a value of 0.27 at the end of test. This trend for rigid boundary gradually increases from an axial strain of about 4% to the end of the test. It found that there is a correlation between the response of average geometrical stability index and fabric anisotropy for both models (see **Figure 11**b). Readers refer to Momeni et al. [7] for more details of average geometrical stability index.

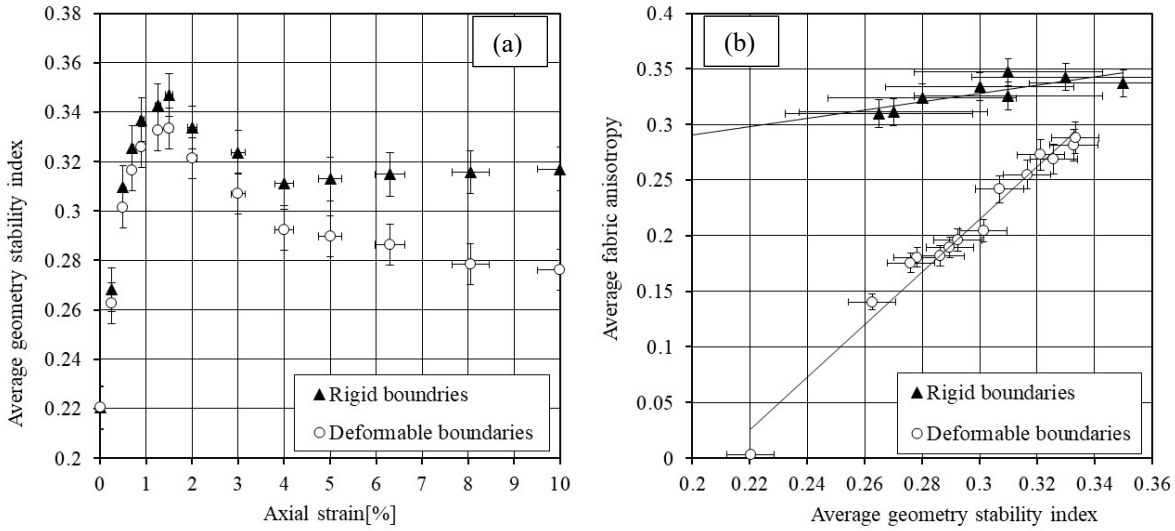

Figure 11 (a)The sensitivity of average geometrical stability index to the different boundary condition, linear coloration between average fabric anisotropy and average geometrical stability index

Figure 12 shows that the trend of deviatoric stress ratio (ratio of axial stress to confining stress) with axial strain between these two models is similar up to an axial strain of about 1%. However, from this point to an axial strain of about 1.5% the sample with the rigid boundary and deformable lateral boundaries reach to a peak deviatoric stress ratio of 2.6 and 2.3, respectively, which is in agreement with the work of Cheung and O'Sullivan [41]. The reason for a higher peak deviatoric stress ratio associated with rigid boundaries is that the lateral movement of the particles is strictly restricted. This results in generating considerable inter-particle and particle-wall contact deformations. That is, the contact forces significantly grow during loading. As a result of this, the sliding capacity of contacts as shown in **Equation 4** significantly increases and consequently the system can take a higher load. Both samples show a notable drop from the peak deviatoric stress ratio up to the axial strain of 4% (i.e. within the softening-strain behaviour). Beyond this axial strain, the deviatoric stress ratio for the model with deformable lateral boundaries has a very slow change, showing the system approaches to the critical state behaviour. However, the stress ratio for the model with rigid lateral boundaries showed growth from the axial strain of 4% to the end of the test, which is not compatible with the typical behaviour of Sand. The volumetric strain behaviour of these two models is demonstrated in **Figure 12**b. Both samples show a contraction in the volumetric strain around the peak deviatoric stress ratio. However, the sample with deformable boundaries shows a slightly larger contraction. The deformable boundaries allow the particles to move freely, therefore, the average coordination number from an axial strain of

0% to 1.5% decreases by about 20%, while this fall is over 12% for the rigid boundary (see **Figure 9**b). That is, the loss of contacts in the case of the rigid boundary is less than that for the deformable boundary. Thus, during the contraction, the sample with the deformable boundary experiences higher contraction. From this axial strain to an axial strain of 3%, both samples partially show a similar dilation behaviour. Changes in the trend of volumetric strain by increasing axial strain beyond this point for the model with deformable boundaries are substantially smaller than that of rigid boundary, indicating the system approaches a critical state behaviour. When soil sample under shearing reaches the critical state behaviour, changes in volumetric and deviatoric stress ratio responses become constant at some point at post-peak (e.g. Wood [4] and Verdugo and Ishihara [46]. In contrast, the trend of volumetric strain shows a rise notably by increasing axial strain for the model with lateral rigid boundaries from an axial strain of about 3% to the end of the test, indicating longer shear and more time is required for the model with rigid boundary to reach the critical state (e.g. Gu, et al. [47] and Nguyen et al. [48]. Soil will reach a unique critical state during shearing, at which it deforms continuously with a constant stress state, constant volumetric state, constant coordination number, constant fabric anisotropy and constant stability index. Tracking these parameters as shear proceeds demonstrates when the soil will reach to the critical state behaviour.

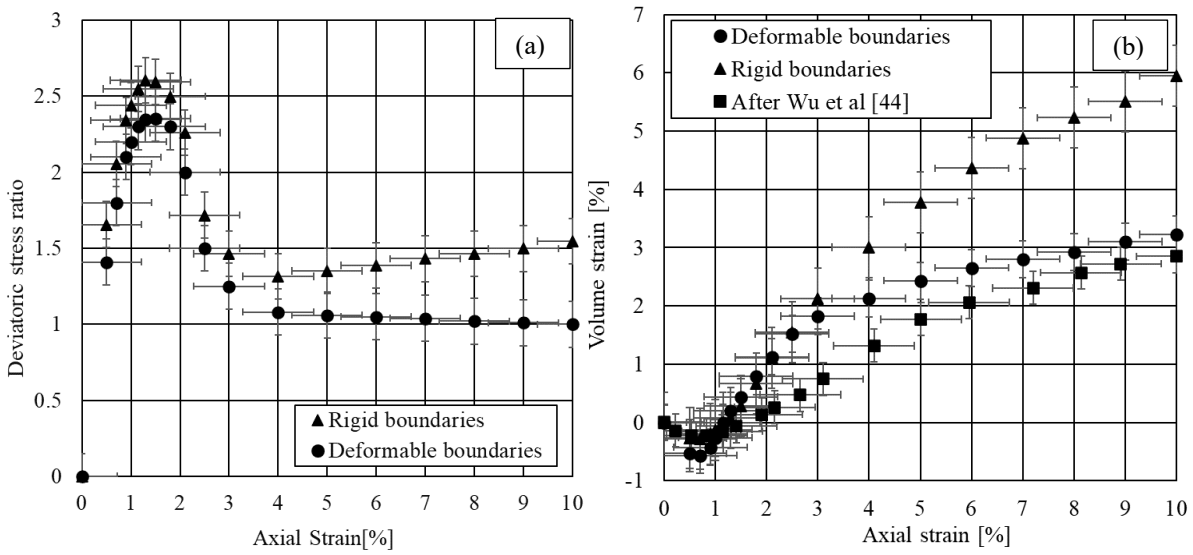

Figure 12 The sensitivity of macro-mechanical behaviour of the system to the different boundary condition: deviatoric stress ratio vs. axial strain, volumetric strain vs. axial strain

The dilation behaviour of the model with deformable boundaries at post-peak is more representative of the typical volumetric behaviour of sand. **Figure 12**b qualitatively compares the volumetric behavior of sand carried out by Wu et al. [44] and the present study. The different between the volumetric behavior of these two works is mainly because of particle size distribution and strain rate. Wu et al. [44] applied a strain rate of 5%/min while in this work it was 2%/min.

Table 2 summaries the sensitivity of macro-mechanical elasto-plastic parameters to the boundary conditions.

Elasto-plastic parameters	Lateral boundary Condition	
	Rigid	Deformable
E (MPa)	35	30

Poisson's ratio	0.18	0.20
∅ (°) (angle of internal friction)	27	24

Table 2 The sensetivity of macro-mechanical elasto-plastic parameters to the boundary condition

The difference between the computed Young's modulus of rigid and deformable boundaries is 17%. This difference between the computed Poisson's ratio between of deformable and rigid boundaries is 11%. As the peak stress for the sample with rigid boundary is higher than that with a deformable boundary, the angle of internal friction for rigid boundary is about 9% bigger than that for the deformable boundary. The angle of internal friction is computed from peak deviatoric stress as follows:

$$\frac{\mathbf{t}}{\mathbf{s}} = \mathbf{Tan^2}\left(\mathbf{45} + \frac{\emptyset}{\mathbf{2}}\right) \qquad \mathbf{(23)}$$

where t is the deviatoric stress and s is the isotropic stress.

7. The sensitivity of Shear band to the lateral boundary conditions

In soil mechanics, shear band refers to a diagonal shear strain localization, characterised by large amount of shear strain [45, 14, 46]. Within this zone, particles experience higher amount of rotation but less movements [41, 14, 7]. Momeni et al. [7] stated that particles which locate within this zone have less contacts compared with the rest of particles and therefore they are less stable. That is, the shear band behaviour is influenced by particle rotations rather than particle displacements [44]. Momeni et al. [7] also showed that those particles that are within this zone have at least two contacts. Sadrekarimi and Olson [47] stated that the onset of shear band is when soil reaches to the elastic limit. In the classical soil mechanics, Coulomb's yield criterion is generally applied to predict the inclination angle of shear band of fine granular materials which is based on the force equilibrium on the failure plane. According to this theory where the ratio of shear stress to normal stress is a maximum at shear only for non-cohesive particulates, the inclination angle of shear band, $\phi_{\boldsymbol{C}}$, can be measured from the direction of minor principal stress, which is orthogonal to the deviatoric stress direction in a biaxial test (see 21.a). The inclination angle of shear band, $\phi_{\boldsymbol{C}}$, can be measured by following empirical relationship:

$$\phi_{\boldsymbol{C}} = \mathbf{45}^\circ + \frac{\emptyset}{\mathbf{2}} \qquad (\mathbf{24})$$

For coarse granular soils, Roscoe theory is applied to predicts the angle of shear band inclination, where dilatancy angle (i.e. $\boldsymbol{\varphi}$) is used to calculate angle of shear band inclination, $\phi_{\boldsymbol{R}}$, [48].

$$\phi_{\boldsymbol{R}} = \mathbf{45}^\circ + \frac{\boldsymbol{\varphi}}{\mathbf{2}} \qquad (\mathbf{25})$$

The significant difference between **Equation (24)** and **Equation (25)** is that the dilatancy angle is much smaller than the angle of internal friction. **Figure 13**(b) to **Figure 13**(f) presents the contour plots of the development of particles displacements during shearing at different axial strain levels for the model with lateral deformable boundaries. As the sample is sheared, a diagonal zone in which the particles displacements are less than the rest of sample is formed. At small axial strain level, the formation of shear band is evident. From axial strain 0.7% to axial strain corresponds to the peak stress (i.e. ε_{11} = 1.5%) the shear band is well formed, and particles experience large amount of displacement. As the bulk dilation increase, the geometry of particles displacements changes notably (e.g. compare particles displacements at ε_{11} = 0.5% and ε_{11} = 1.5%). From ε_{11} = 1.5% to ε_{11} = 10%, two wedges failure forms and particles experience higher displacements. This shear band is qualitatively in a good agreement with that shown in **Figure 13**(g) carried out by Kawamoto et al. [14]. Kawamoto et al. [14] implemented triaxial tests on the coarse sand to study the shear band behaviour, where the samples were isotropically

consolidated to 100[kPa]. They loaded the samples up to axial strain 15% and reported a dilatancy angle and the angle of inclination of shear band of 10° and 50°, respectively. **Figure 13**(h) shows the shear band is clearly formed for the model with lateral rigid boundary at $\varepsilon_{11} = 10\%$. Simple measurements were made to estimate the orientation of the shear band of those models used deformable lateral boundaries and rigid lateral boundaries which are 56° and 62°. With the angle of internal friction provided in **Table 2**, the inclination of the shear band calculated from **Equation (24)** for the model with deformable and rigid boundaries are 57° and 59° respectively. The measured angle of shear band for the model with deformable lateral boundaries is in good agreement with that calculated from **Equation (24)**, while the measured angle of shear band for the model with rigid lateral boundaries is bigger from that calculated from **Equation (24)**. Alshibli and Sture [49] measured shear band thickness using digital imaging techniques by implementing a number of experimental biaxial tests on sands, where the samples were isotropically consolidated to 100[kPa]. They recommended the following empirical relationship to estimate the thickness of shear band:

$$\mathbf{t_s = (10 - 11)\ x\ D_{50}} \qquad \mathbf{(26)}$$

Using simple measurement, the thickness of shear band for the model with deformable and rigid boundaries are 17.5mm and 15mm, respectively. The authors implemented this relationship to estimate the shear band thickness for both models. By applying **Equation (26)**, the thickness of shear band is "10.5x1.7=17.8mm" which is in good agreement with the measured shear band thickness attained from the model with deformable lateral boundaries. It should be noted that in two-dimensional simulation, a particle has three degrees of freedom and is restricted to move and rotate only in-plane while in three-dimensional modelling a particle has six degrees of freedom and is free to move and rotate in any direction without no restriction. Additionally, the number of contacts per particle in 3D models is more than that in 2D models. Hence, longer shear is required that a shear band to be formed for 3D particulate systems in comparison with 2D models. As bulk deformation is restricted in-plane in 2D systems, the 2D models are stiffer than the 3D systems. Chung and O'Sullivan [41] qualitatively studied the shear behaviour of particulate soils under 2D biaxial and 3D triaxial simulations using DEM. They showed that those particles that fall within the shear band in 2D systems experience more rotation in comparison with particles' rotation within the shear band in 3D systems. They also indicated that the bulk shear capacity of particulate soils in 3D systems is greatly dependent on the particles' rotation in radial directions such that particles that fall into the shear band experience similar values of rotation in lateral radial directions.

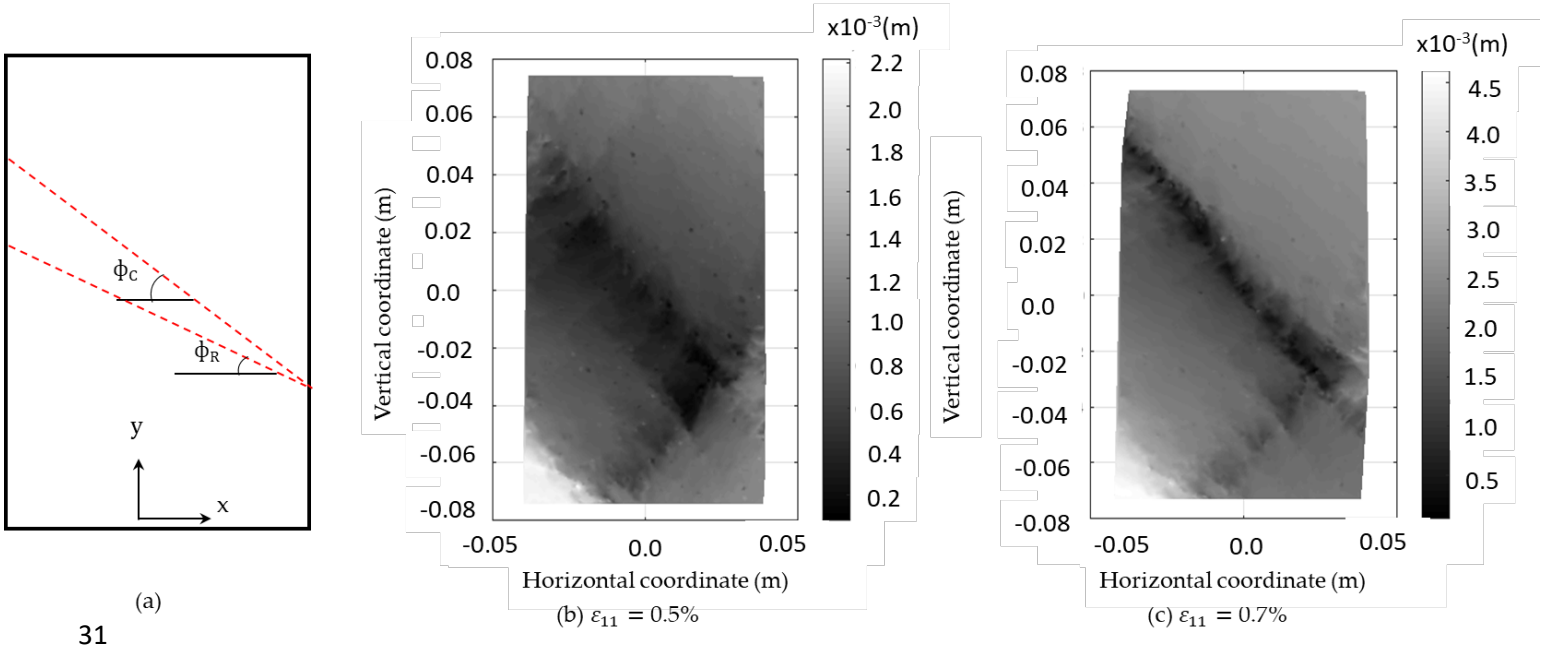

(a)

(b) $\varepsilon_{11} = 0.5\%$

(c) $\varepsilon_{11} = 0.7\%$

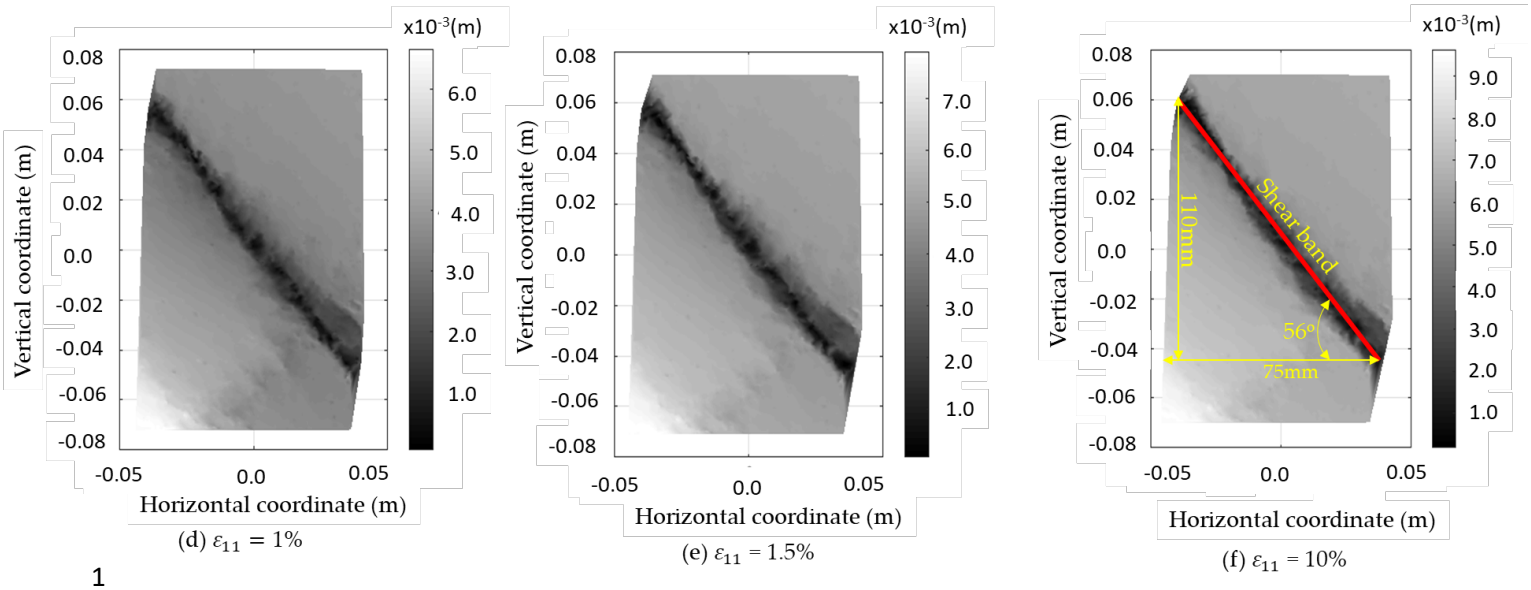

(d) ε_{11} = 1% (e) ε_{11} = 1.5% (f) ε_{11} = 10%

1

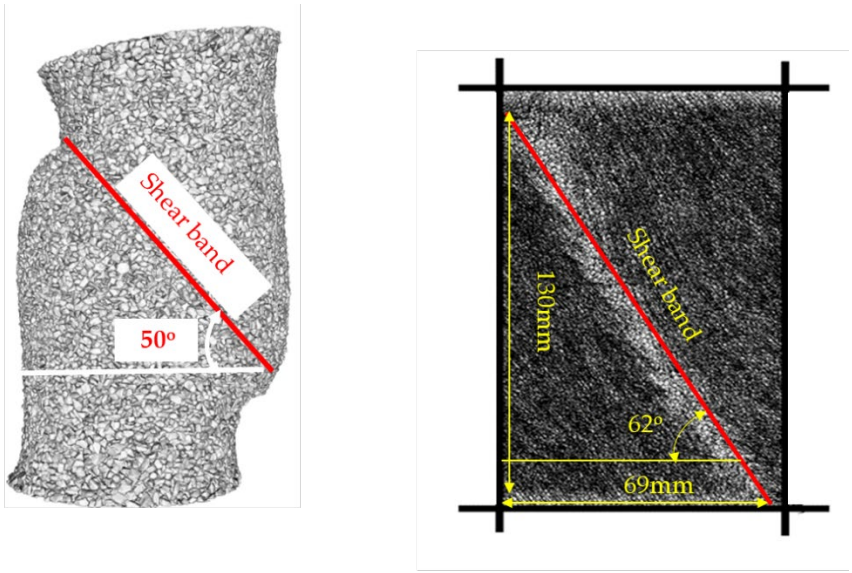

(g) At ε_{11} = 15% (After Kawamoto et al. [14]) (h) ε_{11} = 10%

2

3 Figure 13 (a) shear band inclination angle based on Coulomb and Roscoe theories, (b to f) Evolution of shear
4 band during shearing for deformable lateral boundaries, (g) Experimental shear band formation at axial strain
5 15% (Kawamoto et al. **[14]**) and (h) shear band formation at axial strain 15% for rigid lateral boundaries. The grey
6 bar is displacement.

7 **8. Conclusion**

8 An algorithm to implement the deformable lateral boundaries for the 2D DEM biaxial test is presented
9 in this paper where the micro-mechanical behaviors of particles are studied, and compared with the
10 case of rigid boundaries:

11 - Tracking the variation of average fabric anisotropy shows that from axial strain of about 1.5%
12 onwards, the average fabric anisotropy for both systems reduces, indicating the particulate
13 systems are not able to develop more contacts per particle to take the higher major principal
14 stress. This drop in average fabric anisotropy from axial strain 1.5% onwards is more notable
15 for the model with deformable boundary particles.

- It is found that the model with rigid boundaries leads to higher value of average fabric anisotropy and average geometrical stability index. In particular, as the sample is sheared, after the peak stress the instability index constantly reduces to the end of the test for the model with deformable boundaries, while rigid boundaries shows a slight increase of average geometrical stability index after a strain of about 4%.

- Tracing the evolution of particle movements during shearing for the model with deformable lateral boundaries shows the angle of inclination of the shear band 23develops long before peak stress is achieved. The measured thickness of the shear band and inclination of the shear band from the model with deformable lateral boundaries are in good agreement with the value of shear band thickness and inclination of shear band calculated from empirical equations.

The DEM modeling tests suggest that the developed algorithm for the deformable boundary could improve the accuracy of modeling soil samples and can better represent the actual behavior of granular soils.

9. References

[1] B. Das, "Soil mechanics laboratory manual," New York, USA, Oxford University Press, 2002, pp. 99-108.

[2] K. Head, "Manual of soil laboratory testing (Vol. 1, No. 2)," Pentech press, London, 1980.

[3] T. a. W. R. Lambe, Soil mechanics, New York: John Willey & Sons. Inc, 1969.

[4] D. Wood, Soil behaviour and critical state soil mechanics, Cambridge : Cambridge university press, 1990.

[5] P. a. S. O. Cundall, "A discrete numerical model for granular assemblies. , G," *geotechnique,* vol. 29, no. 1, pp. 47-65, 1979.

[6] J. T. J. a. M. H. Kozicki, "Discrete simulations of a triaxial compression test for sand by DEM," *International Journal for Numerical and Analytical Methods in Geomechanics,* vol. 38, no. 18, pp. 1923-1952, 2014.

[7] A. C. B. a. S. Y. Momeni, "An Introduction to the Geometrical Stability Index: A Fabric Quantity," *Geotechnics,* vol. 2, no. 2, pp. 297-316, 2022.

[8] M. N.-N. S. a. K. J. Oda, "Stress-induced anisotropy in granular masses," *Soils and foundations,* vol. 25, no. 3, pp. 85-97, 1985.

[9] L. a. B. R. Rothenburg, "Analytical study of induced anisotropy in idealized granular materials.," *Geotechnique,* vol. 39, no. 4, pp. 601-614, 1989.

[10] L. a. K. N. Rothenburg, "Critical state and evolution of coordination number in simulated granular materials," *International Journal of Solids and Structures,* vol. 41, no. 21, pp. 5763-5774, 2004.

[11] A. C. F. I. T. a. L. J. Fakhimi, "Simulation of failure around a circular opening in rock," *International Journal of Rock Mechanics and Mining Sciences,* vol. 39, no. 4, pp. 507-515, 2002.

[12] F. M. C. a. D. F. Camborde, "Numerical study of rock and concrete behaviour by discrete element modelling," *Computers and geotechnics,* vol. 27, no. 4, pp. 225-247, 2000.

[13] M. K. H. a. K. J. Oda, "Effects of induced anisotropy on the development of shear bands in granular materials.," *Mechanics of materials,* vol. 28, no. 1, pp. 103-111, 1998.

[14] R. A. E. V. G. a. A. J. Kawamoto, "All you need is shape: Predicting shear banding in sand with LS-DEM," *Journal of the Mechanics and Physics of Solids,* vol. 111, pp. 375-392, 2018.

[15] Itasca, "Particle Flow Code 2D (PFC2D)," Itasca, Minneapolis, USA, 2014.

[16] K. a. O. M. Iwashita, "Rolling resistance at contacts in simulation of shear band development by DEM," *Journal of engineering mechanics,* vol. 124, no. 3, pp. 285-292, 1998.

[17] M. a. I. K. Oda, "Mechanics of granular materials: an introduction," *CRC press,* 2020.

[18] C. a. Z. L. Thornton, "Numerical simulations of the direct shear test," *Chemical Engineering & Technology,* vol. 26, no. 2, pp. 153-156, 2003.

[19] T. Sitharam, "Discrete element modelling of cyclic behaviour of granular materials," *Geotechnical & Geological Engineering,* vol. 21, no. 4, pp. 297-329, 2003.

[20] D. a. C. P. Potyondy, "A bonded-particle model for rock," *International journal of rock mechanics and mining sciences,* vol. 41, no. 8, pp. 1329-1364, 2004.

[21] C. D. B. J. a. L. S. O'Sullivan, "A new approach for calculating strain for particulate media," *International Journal for numerical and analytical methods in geomechanics,* vol. 27, no. 10, pp. 859-877, 2003.

[22] C. O'Sullivan, Particulate discrete element modelling, Taylor & Francis, 2011.

[23] X. H. K. O. C. a. K. C. Huang, "Implementation of rotational resistance models: A critical appraisal.," *Particuology,* vol. 34, pp. 14-23, 2017.

[24] P. Y. Z. Z. W. a. C. W. Wang, "Micro-mechanical analysis of soil–structure interface behavior under constant normal stiffness condition with DEM," *Acta Geotechnica,* vol. 17, no. 7, pp. 2711-2733, 2022.

[25] K. J. a. K. Johnson, Contact Mechanics, Cambridge University Press, 1987.

[26] L. &. B. R. Rothenburg, "Analytical Study of Induced Anisotropy in Idealized Granular Materials.," vol. 39, pp. 601-614, 1989.

[27] L. Rothenburg, "Micromechanics of idealized granular assemblies," PhD Thesis , University of Waterloo, Canada, 1980.

[28] R. M. German, "Coordination Number Changes During Powder Densification," vol. 253, p. 368–376, 2014.

[29] T. Ng, "Fabric Evolution of Ellipsoidal Arrays With Different Particle Shapes.," vol. 127, pp. 994-999, 2001.

[30] L. a. K. N. Rothenburg, "Critical state and evolution of coordination number in simulated granular materials," *International Journal of Solids and Structures,* vol. 41, no. 21, pp. 5763-5774, 2004.

[31] K. Maeda, "Critical State-based Geo-micromechanics on Granular Flow," *American Institute of Physics,* vol. 1145, no. 1, pp. 17-24, 2009.

[32] A. Momeni, "Micro-mechanical study of sand fabric during earthquake (Doctoral dissertation)," University of Leeds, Leeds, UK, 2014.

[33] R. G. M. a. A. S. Moreno, "Effect of the impact angle on the breakage of agglomerates: a numerical study using DEM," *Powder Technology,* vol. 130, no. 1, pp. 132-137, 2003.

[34] N. P. J. D. F. D. F. a. S. A. Belheine, "Numerical simulation of drained triaxial test using 3D discrete element modeling," *Computers and Geotechnics,* vol. 36, no. 1-2, pp. 320-331, 2009.

[35] C. a. A. S. Thornton, "Quasi-static shear deformation of a soft particle system," *Powder technology,* vol. 109, no. 1, pp. 179-191, 2000.

[36] L. O. C. a. O. S. Cui, "An analysis of the triaxial apparatus using a mixed boundary three-dimensional discrete element model," *Geotechnique,* vol. 57, no. 10, pp. 831-844, 2007.

[37] U. a. D. C. El Shamy, "Microscale characterization of energy dissipation mechanisms in liquefiable granular soils," *Computers and Geotechnics,* vol. 37, no. 7, pp. 846-857, 2010.

[38] N. a. E. S. U. Zamani, "Analysis of wave propagation in dry granular soils using DEM simulations," *Acta Geotechnica,* vol. 6, no. 3, pp. 167-182, 2011.

[39] Itasca, "Particle Flow Code in Three Dimensions," Itasca, Minneapolis, USA, 2014.

[40] Y. a. L. S. Wang, "Characterization of cemented sand by experimental and numerical investigations," *Journal of geotechnical and geoenvironmental engineering,* vol. 134, no. 7, pp. 992-1004, 2008.

[41] G. a. O. C. Cheung, "Effective simulation of flexible lateral boundaries in two-and three-dimensional DEM simulations," *Particuology,* vol. 6, no. 6, pp. 483-500, 2008.

[42] J. O. C. a. M. G. O'Donovan, "Two-dimensional discrete element modelling of bender element tests on an idealised granular material.," *Granular Matter,* vol. 14, no. 6, pp. 733-747, 2012.

[43] Y. L. C. B. B. &. T. C. Sheng, "Numerical Studies of Uniaxial Powder Compaction Process By 3D DEM.," vol. 21, pp. 304-317, 2004.

[44] K. L. S. S. W. R. S. Wu, "DEM study of the shear behavior and formation of shear band in biaxial," *Adv. Powder Technol,* vol. 31, pp. 1431-1440, 2020.

[45] J. a. C. R. Desrues, "Shear band analysis and shear moduli calibration," *International Journal of Solids and Structures,* vol. 39, no. 13-14, pp. 3757-3776, 2002.

[46] V. a. S. H. Galavi, "Nonlocal multilaminate model for strain softening analysis," *International Journal of Geomechanics,* vol. 10, no. 1, pp. 30-44, 2010.

[47] A. a. O. S. Sadrekarimi, "Shear band formation observed in ring shear tests on sandy soils," *Journal of geotechnical and geoenvironmental engineering,* vol. 136, no. 2, pp. 366-375, 2010.

[48] P. A. Vermeer, "The orientation of shear band in biaxial tests," *Geotechnique,* vol. 40, no. 2, pp. 223-236, 1990.

[49] K. a. S. S. Alshibli, "Sand shear band thickness measurements by digital imaging techniques," *Journal of computing in civil engineering,* vol. 13, no. 2, pp. 103-109, 1999.

[50] C. B. J. a. R. M. O'Sullivan, "Influence of particle shape and surface friction variability on response of rod-shaped particulate media.," *Journal of Engineering Mechanics,* vol. 128, no. 11, pp. 1182-1192, 2002.

1

2

Nomenclature

$\dot{\boldsymbol{x}}$ translational Particle velocity $\dot{\boldsymbol{\theta}}$ rotational Particle velocity

θ_a rotation of $E(\theta)$ θ_n direction of $\bar{\boldsymbol{f}}_{\boldsymbol{n}}^{\boldsymbol{c}}(\boldsymbol{\theta})$

$\bar{\boldsymbol{f}}_{\boldsymbol{0}}^{\boldsymbol{c}}$ average normal forces C_n Average coordination number

$\boldsymbol{\Delta_n}$ Normal contact deformation a Fabric anisotropy

Δ_t Time step $\boldsymbol{\Delta_s}$ Shear contact deformation

θ Angle of contact force from x-axis and angle friction

α Damping constant $\dot{\varepsilon}$ Strain rate

K_s Tangential contact stiffness K_n Normal contact stiffness

$\boldsymbol{F_i^n}$ Total normal contact force $\boldsymbol{F_i^s}$ Total tangential contact force

ρ Particle density $\dot{\varepsilon}$ Strain rate

p_y Contact pressure I density scaling factor

$\boldsymbol{F_i}$ contact force a_n normal contact force anisotropy

F Resultant force **M** Torque

$\boldsymbol{F_i^d}$ Local damping force $\boldsymbol{n}$ and $\boldsymbol{t}$ unite vector

v Particle velocity and Poisson's ratio

R Particle radius ϕ_C Angle of shear band: Coulomb's theory

t Deviatoric stress s Isotropic stress

E Young's Modulus ϕ_R Angle of shear band: Roscoe's theory

ε_{11} Major Strain tensor component in axial direction

ε_v Volumetric strain φ dilatancy angle

D_{50} Mean particle size t_s thickness of shear band

μ coefficient of friction $\mathbf{u_x}$ Particle velocity in x-direction

$\mathbf{u_y}$ Particle velocity in y-direction σ_t Target stress